Electromagnetic moments of odd-A $^{193–203,211}$Po isotopes

M. D. Seliverstov,[1,2,3,4,*] T. E. Cocolios,[1,5,6] W. Dexters,[1] A. N. Andreyev,[4,7] S. Antalic,[8] A. E. Barzakh,[2] B. Bastin,[1] J. Büscher,[1] I. G. Darby,[1] D. V. Fedorov,[2] V. N. Fedosseev,[5] K. T. Flanagan,[9,10] S. Franchoo,[11] G. Huber,[3] M. Huyse,[1] M. Keupers,[1] U. Köster,[12] Yu. Kudryavtsev,[1] B. A. Marsh,[5] P. L. Molkanov,[2] R. D. Page,[13] A. M. Sjödin,[5,14] I. Stefan,[11] P. Van Duppen,[1,5] M. Venhart,[1,15] and S. G. Zemlyanoy[16]

[1]*KU Leuven, Instituut voor Kern- en Stralingsfysica, B-3001 Leuven, Belgium*
[2]*Petersburg Nuclear Physics Institute, NRC Kurchatov Institute, 188300 Gatchina, Russia*
[3]*Institut für Physik, Johannes Gutenberg Universität, D-55099 Mainz, Germany*
[4]*Department of Physics, University of York, York YO10 5DD, United Kingdom*
[5]*CERN, CH-1211 Geneva 23, Switzerland*
[6]*Department of Physics, University of Manchester, M60 1AD Manchester, United Kingdom*
[7]*Advanced Science Research Centre (ASRC), Japan Atomic Energy Agency (JAEA), Tokai-mura, Ibaraki 319-1195, Japan*
[8]*Department of Nuclear Physics and Biophysics, Comenius University, 842 48 Bratislava, Slovakia*
[9]*Department of Physics, University of Manchester, M13 9PL Manchester, United Kingdom*
[10]*Centre de Spectrométrie Nucléaire et de Spectrométrie de Masse, F-91405 Orsay, France*
[11]*Institut de Physique Nucléaire, F-91406 Orsay, France*
[12]*Institut Laue-Langevin, F-38042 Grenoble, France*
[13]*Oliver Lodge Laboratory, University of Liverpool, L69 7ZE Liverpool, United Kingdom*
[14]*KTH–Royal Institute of Technology, SE-10044 Stockholm, Sweden*
[15]*Institute of Physics, Slovak Academy of Sciences, 845 11 Bratislava, Slovakia*
[16]*Joint Institute of Nuclear Research, 141980 Dubna, Moscow Region, Russia*

(Received 15 January 2014; published 31 March 2014)

Hyperfine splitting parameters have been measured for the neutron-deficient odd-mass polonium isotopes and isomers $^{193–203}$Po^{g,m}, ^{209,211}Po. The measurement was performed at the ISOLDE (CERN) online mass separator using the in-source resonance ionization spectroscopy technique. The magnetic dipole moments μ and spectroscopic electric quadrupole moments Q_S have been deduced. Their implication for the understanding of nuclear structure in the vicinity of the closed proton shell at $Z = 82$ and the neutron mid-shell at $N = 104$ is discussed. For the most neutron-deficient nuclei ($A = 193,195,197$), a deviation of μ and Q_S from the nearly constant values for heavier polonium nuclei was observed. Particle-plus-rotor calculations with static oblate deformation describe the electromagnetic moments for these nuclei well, provided a gradual increase of a mean deformation when going to lighter masses is assumed for the polonium nuclei with $A < 198$.

DOI: 10.1103/PhysRevC.89.034323 PACS number(s): 21.10.Ky, 27.80.+w, 29.38.−c, 31.30.Gs

I. INTRODUCTION

The interest in experimental and theoretical studies of shape coexistence at low energy in nuclei has been continuously growing [1–5]. The region around $N = 104$ (neutron mid-shell between $N = 82$ and $N = 126$) and the closed proton shell at $Z = 82$ is especially prolific in this respect. From an experimental point of view the effects of shape-coexistence and shape-transition are well known for mercury isotopes ($Z = 80$) around $N = 104$. These phenomena are manifested, among other observables, by the large odd-even staggering in the charge radii [6]. More recently, the studies in the long chain of the lead ($Z = 82$) isotopes revealed that these nuclei remain essentially spherical in their ground states down to $N = 102$ [7,8] despite the presence of low-lying states with different shapes [3].

Low-lying intruder states of a similar nature to those in the lead isotopes have been previously identified in polonium [4,9]. In our recent work [10,11] changes in the mean-square charge radii $\delta\langle r^2\rangle$ were measured for a wide range of polonium isotopes (ground states and long-lived isomers) from $A = 191$ to $A = 218$. Combined analysis of the data for the even-A and odd-A polonium isotopes leads to the conclusion that an onset of deformation occurs at ^{197,198}Po, which is significantly earlier (when going away from magic neutron number $N = 126$) than has been suggested by previous experimental and theoretical studies (e.g., Ref. [4]). The extracted charge radii indicate a deviation from sphericity for ground and isomeric states of the lightest odd- and even-A polonium isotopes with $A \leqslant 197$, unlike the mercury isotopic chain, where even-A isotopes remain nearly spherical at least down to $A = 182$ [6]. A comparison of the relative $\delta\langle r^2\rangle$ values with those for the isotones in the lead and mercury isotopic chain (see Fig. 6 from Ref. [11]) shows that deformation sets in much earlier for the isotopes with extra protons above the $Z = 82$ closure compared to their isotones below $Z = 82$ [10,11].

In this paper, we present the electromagnetic moments deduced from the same data set as used in our previous work [10,11] for the extraction of charge radii. These new data will elucidate the evolution of shape coexistence in this region of the nuclear chart.

*maxim.seliverstov@cern.ch

II. EXPERIMENTAL DETAILS

A. Beam production

The experiments were performed at the ISOLDE facility (CERN) [12]. Beams of $^{193–199}$Po were produced in the first experimental campaign (Run I, 2007) and beams of $^{193–195,201,203,209,211}$Po were produced in the second campaign (Run II, 2009). The polonium nuclei were produced in spallation reactions induced by the 1.4-GeV proton beam (intensity up to 2 μA) from the CERN PS Booster impinging on a UC_x target (50 g/cm^2 of ^{238}U). The spallation products effused out of the high temperature target ($T \approx 2050\,^\circ$C) as neutral atoms into the cavity of the Resonance Ionization Laser Ion Source, RILIS [13,14]. The polonium atoms were resonantly ionized within this cavity when the laser beams were wavelength-tuned to the three-step polonium ionization scheme (see Fig. 1).

Laser light for the resonant excitation of the first two atomic transitions was provided by two tunable pulsed dye lasers. The ultraviolet radiation was obtained by tripling the frequency of the fundamental dye laser radiation using β-barium borate (BBO) crystals. Copper vapor lasers (CVL) operating at a pulse repetition rate of 11 kHz (Run I) and a Nd:YAG laser operating at 10 kHz (Run II) were used to pump the dye lasers and to perform the transition from the second excited state into the continuum (the third step). The use of a single powerful Nd:YAG laser (total power of 100 W) instead of the copper vapor oscillator-amplifier laser system resulted in an improved photoionization stability [15]. The photoionization efficiency for polonium atoms was estimated as 0.5–1%.

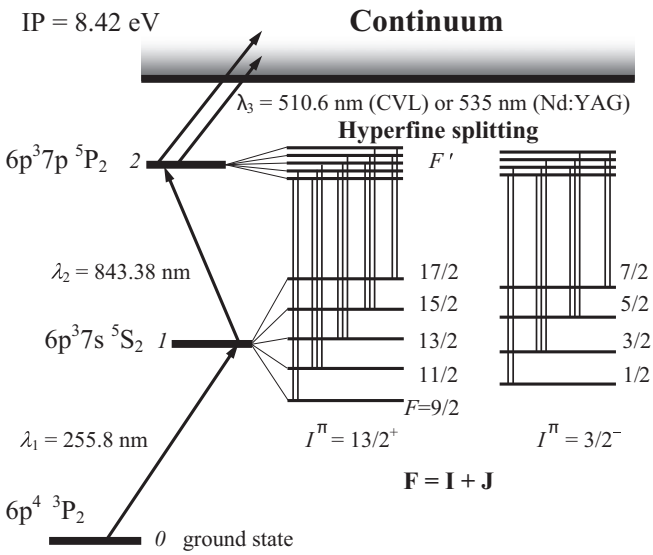

FIG. 1. The three-step laser-ionization scheme for polonium [16]. The electronic configurations for the levels involved and the laser wavelengths for each step are shown. The hyperfine structures for the $13/2^+$ and $3/2^-$ states of odd-A polonium isotopes are shown schematically (not to scale). The hyperfine lines expected for $I = 13/2$, $I = 3/2$ are also shown.

B. Radioactive beam identification and counting

After selective laser photoionization in the hot cavity, the radioactive ions of interest were extracted and accelerated to 30 keV (Run I) or to 50 keV (Run II), mass separated and subsequently distributed to counting stations (Faraday cup, Windmill chamber, or tape station) according to beam intensity and decay mode. More details of different ion-detection techniques at ISOLDE are given in Ref. [17].

1. Faraday cup

Direct ion-counting with a Faraday cup is, in general, the simplest and most universal way of detecting photoions, provided the ion beam is intense and isobarically pure. The ion beam intensity of ^{209}Po was sufficient ($\sim$1 pA) to be measured directly with a Faraday cup after the mass separator, but surface-ionized isobaric ^{209}Fr was also present in the beam and prevented the direct counting of the polonium ions. A large fraction of the polonium beam originated from the decay of ^{209}At which was also produced in the spallation reactions and trapped in the target material. The francium isobar has no long-lived precursor in the target and releases completely from the target material in a few minutes. This allowed ^{209}Po to be studied in a pseudo-offline mode, whereby the proton-beam irradiation was stopped once the target had been sufficiently long (several hours) irradiated to provide a usable sample of the precursor isotopes.

2. Windmill

The short-lived α-decaying isotopes $^{193–197,211}$Po were detected using their characteristic α decay. The mass-separated beams were sent to the Windmill chamber, where the ions were implanted into one of ten carbon foils (20 μg/cm^2) [18] mounted on a wheel. An illustration of the Windmill setup is shown in Fig. 2. The implantation site was surrounded by two circular silicon detectors, one of which was of an annular type that allowed the beam to pass through. The annular detector with an active area of 450 mm^2, thickness of 300 μm, and a central hole with a diameter of 6 mm, was positioned at a distance of $\sim$7 mm upstream; the standard detector with active area 300 mm^2 and thickness 300 μm was placed $\sim$4 mm downstream of the foil. The total detection efficiency of the detectors setup was estimated to be 51% for α particles. The second detector pair was located at off-beam-axis position and used for detection of α decays of previously implanted ions.

A typical α-decay energy spectrum obtained at $A = 197$ is shown in Fig. 3. The α decay of the isomer and ground state of ^{197}Po can be observed. The peak full width at half maximum (FWHM) is 30 keV. For $^{193–197,211}$Po by using α-decay analysis it was possible to identify the isotopes, to discriminate possible isobaric contaminants, and to discriminate the low-spin and high-spin isomers.

The Windmill can also be surrounded by two high-purity germanium detectors, placed behind and to the side of the vacuum chamber, allowing charged-particle–γ-ray coincidences to be studied [19].

The low background and high efficiency of the α-particle detection at the Windmill station enabled laser-spectroscopy

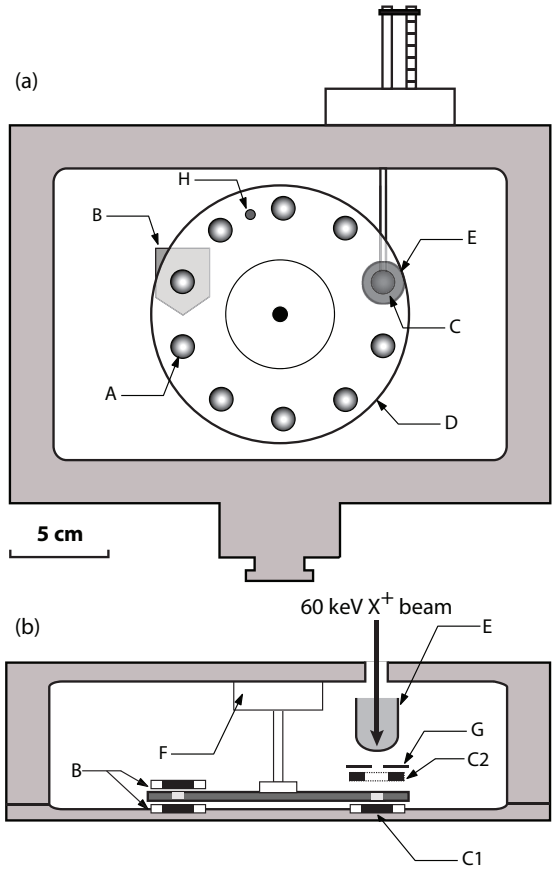

FIG. 2. (Color online) Schematic of the Windmill detection chamber: (a) frontal view, (b) top view. The beam is implanted into one of 10 carbon foils A (20 μg/cm^2) mounted on a rotating wheel D which is controled by a stepper motor F. The α decay is monitored using silicon detectors, either at the implantation site C or at the decay position B. The implantation site has annular detector $C2$ with a hole (hole diameter of 6 mm) in the middle to allow the beam to pass. A retractable, secondary-electron-suppressed Faraday cup E is used for beam tuning and monitoring. Detector $C2$ is protected by a collimator G. The reference ^{241}Am α sources (<50 Bq) H are placed between two foil positions on either side of the wheel to monitor the performance of the silicon detectors at the positions B and C in the course of an experimental campaign.

measurements of isotopes with an extremely low production yield (<0.1 s^{-1} for ^{191}Po [11]).

3. Tape station

The isotopes $^{199–203}$Po have a smaller α-decay branch and a longer half-life than the lighter isotopes studied with the Windmill setup. The resulting α-decay energy spectra have therefore limited statistics and carry the contamination of a previous implantation even after the time elapsed between two implantations on the same foil (up to 600 s). Those isotopes were instead detected by measuring the intensity of their characteristic γ-ray emission at the ISOLDE identification tape station [20].

The ion beam was implanted on a tape for a set time, and then the tape was moved in front of a 4π plastic scintillator

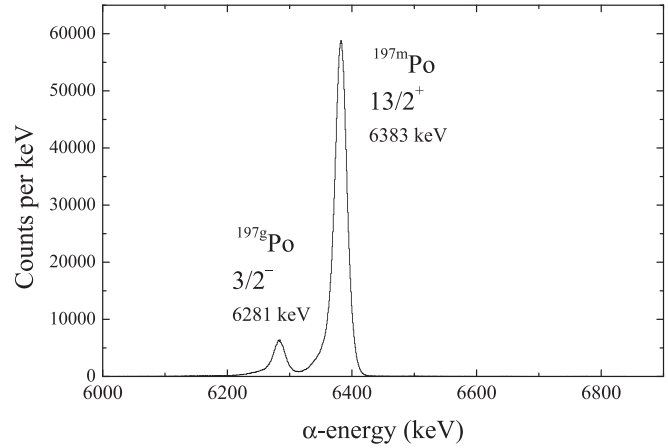

FIG. 3. Example of α-decay energy spectrum for ^{197}Po collected at the Windmill decay station. Decay spectra for ^{191}Po are in Ref. [11] and for ^{195}Po in Ref. [19].

detector (for the detection of β particles) and a single high-purity germanium detector. This setup is well suited for the study of isotopes with half-lives from tens of seconds to several minutes.

A typical γ-ray energy spectrum collected using the Ge detector at the tape station is shown in Fig. 4. The application of the high-resolution germanium detector allowed the identification of γ rays specific to the decay of the low-spin and high-spin isomers.

C. In-source laser spectroscopy

For the atomic spectroscopy measurements, a narrow-bandwidth laser (linewidth of 1.2 GHz) was used for the second excitation step ($\lambda_2 = 843.38$ nm). A broadband laser (>20 GHz) was used for the first step to cover the hyperfine structure and isotope shift across the whole isotopic chain (see Fig. 1). The laser power for the second excitation step was reduced to avoid line broadening caused by saturation.

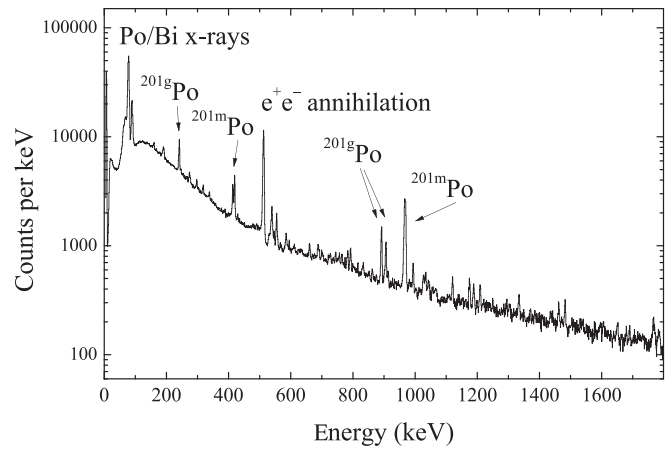

FIG. 4. Example of γ-ray energy spectrum for ^{201}Po collected at the tape station. Decay spectra for ^{199}Po are in Ref. [21].

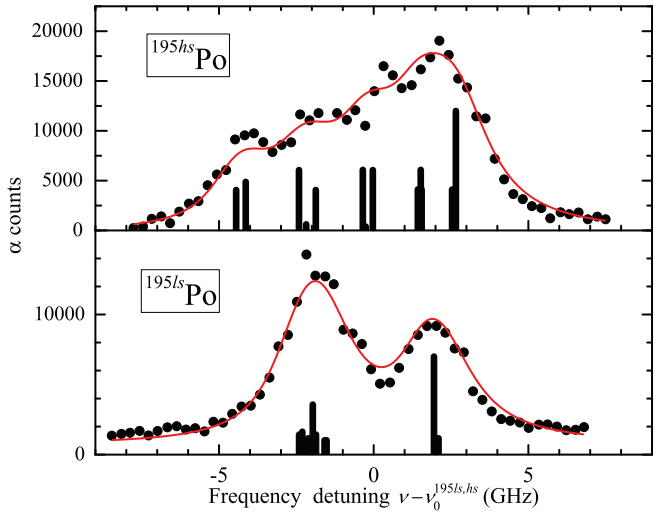

FIG. 5. (Color online) Dependence of the number of the detected photoions (deduced from the number of α particles, $E_\alpha^{ls} = 6606$ keV, $E_\alpha^{hs} = 6699$ keV) on the laser frequency detuning. Frequency detuning is shown with respect to the hfs centroids of the high-spin state ^{195hs}Po [$I^\pi = (13/2^+)$] and the low-spin state ^{195ls}Po [$I^\pi = (3/2^-)$]. Solid lines represent a fit to the data (see text). The calculated positions and relative intensities of the individual hyperfine components are shown with vertical bars.

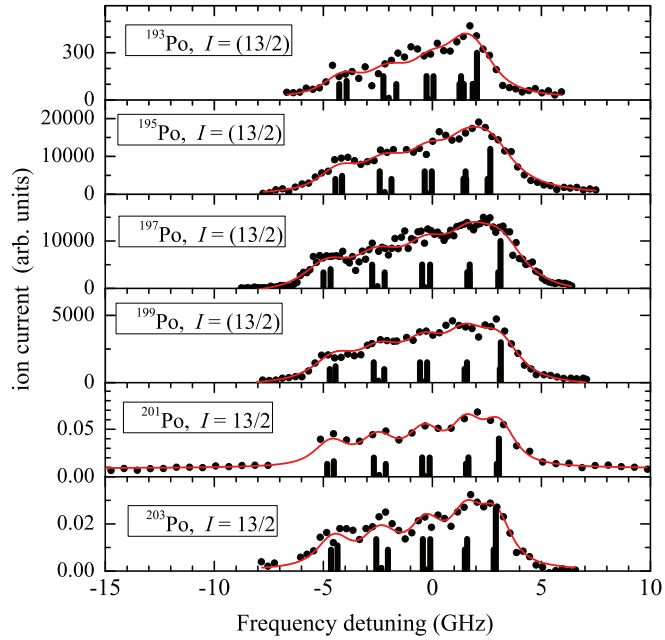

FIG. 6. (Color online) Similar to Fig. 5, but for high-spin states of polonium isotopes. Frequency detuning is shown with respect to the centroids of each hfs.

The counting of the photoions/decays and the stepwise change of the laser frequency were synchronized with selected proton pulses from the CERN PS Booster beam delivery cycles ("supercycles") [22], consisting of a sequence of 12 to 45 proton pulses, 2.4 μs wide and separated by 1.2 s, which were distributed to different experiments. The full acquisition cycle at each frequency step (laser frequency change, beam implantation, photoion/decay counting) was carried out over an integer number of supercycles. After the counting cycle was complete, the ISOLDE beam delivery was stopped and then the laser frequency was tuned to the subsequent step.

Examples of the optical spectra for the ground and isomeric states of ^{195}Po collected in the same laser scan are shown in Fig. 5. The optical spectra obtained for the high-spin states of $^{193–203}$Po ($I = 13/2$) are shown in Fig. 6.

III. DATA ANALYSIS

A. Position and relative intensities of hfs components

The atomic spectroscopic measurements have been performed using the $6p^3 7s\ ^5S_2 \longrightarrow 6p^3 7p\ ^5P_2$ ($\lambda_2 = 843.38$ nm) transition (see Fig. 1). The positions of the hyperfine components $\nu^{F,F'}$ are determined by:

$$\nu^{F,F'} = \nu_0 + \Delta\nu^{F'} - \Delta\nu^{F}, \tag{1}$$

where ν_0 is the position of the center of gravity of the hyperfine structure, the prime symbol denotes the upper level of the transition, and

$$\Delta\nu^{F} = A\frac{C}{2} + B\frac{\frac{3}{4}C(C+1) - I(I+1)J(J+1)}{2(2I-1)(2J-1)IJ}, \tag{2}$$

where I is the nuclear spin, J is the atomic spin, $C = F(F+1) - I(I+1) - J(J+1)$, F is the total angular momentum of the atom ($\mathbf{F} = \mathbf{I} + \mathbf{J}$), and A and B are the magnetic dipole and electric quadrupole hyperfine coupling constants, respectively.

The experimental optical spectra were fitted with a convolution of a Gaussian Doppler profile N_G, representing the thermal distribution of atomic velocities corresponding to the ion source temperature, and P_{ion}, representing the probability of photoionization, which depends on the spectral density of the laser power. In a general form the number of photoionized atoms for an individual hfs transition can be presented as

$$N_{\text{ion}}(\nu) = N_0 \int N_G(\nu')P_{\text{ion}}(\nu - \nu')d\nu'. \tag{3}$$

In a simple case (two-step photoinization scheme, well resolved hfs components, absence of saturation of all transitions) the photoionization probability P_{ion} is proportional to the spectral density of the laser power I_L and can be presented as

$$P_{\text{ion}}(\nu - \nu') \sim \sum S_{FF'} I_L(\nu + \Delta\nu^{FF'} - \nu'), \tag{4}$$

where $S_{FF'}$ is the relative probability of the transition,

$$S_{FF'} \sim (2F+1)(2F'+1)\begin{Bmatrix} J' & F' & I \\ F & J & 1 \end{Bmatrix}^2, \tag{5}$$

and $\{\dots\}$ is the Wigner $6j$ symbol. In the fitting procedure an asymmetric Lorenzian profile was used for I_L and the asymmetry parameter was deduced from fitting the spectra of the even-A isotopes ($I = 0$, single-line optical spectrum), obtained in the same experiment [10].

To take into account the saturation of transitions, pumping processes between hfs structure components and a population redistribution of the hfs levels, the number of photoions for each frequency step was calculated by solving the rate equations for the given photoionization scheme:

$$\begin{aligned} \frac{dN_F}{dt} &= \sum_k W_{F'_kF} N_{F'_k} - \sum_k W_{FF'_k} N_F - W_{F,\mathrm{ion}} N_F, \\ &\vdots \\ \frac{dN_{\mathrm{ion}}}{dt} &= \sum_k W_{F'_k,\mathrm{ion}} N_{F'_k}, \end{aligned} \tag{6}$$

where N_F is the population of hfs sublevels, and $W_{FF'}$ is the transition rate between sublevels F and F':

$$W_{FF'} \sim S'_{FF'} I_L(\nu + \Delta\nu^{FF'} - \nu'), \tag{7}$$

where $S'_{FF'} = S_{FF'}/(2F+1)$. For the first and ionization transitions the spectral density of the laser power does not depend on the frequency. The population of the ground-state sublevels at $t = 0$ is proportional to their statistical weights $N_F^0 \sim 2F + 1$. The relative intensities of the hfs line shown with the vertical bars in Figs. 5 and 6 were calculated using Eq. (5) and are presented as an illustration only.

B. Hyperfine splitting parameters

The parameters ν_0, A, and B were varied during the fitting routine, and the ratios A'/A and B'/B were fixed, neglecting the hfs anomaly, which is usually less than 10^{-3}. The ratio A'/A (corresponding to A_2/A_1, according to the level numbering from Fig. 1) was constrained to the value $(A_2/A_1)_{\mathrm{exp}} = 0.06(1)$ deduced from fitting the spectra of ^{209}Po ($I = 1/2, B = 0$) with fixed hfs coupling constant $A_1^{209} = 2127(3)$ MHz [23].

In fitting the spectra of the polonium isotopes with $I > 1/2$ the ratio B'/B was constrained to

$$\left(\frac{B_2}{B_1}\right)_{\mathrm{calc}} = \left(\frac{B_0}{B_1}\right)_{\mathrm{ref}} \times \left(\frac{b_2^{7p}}{b_0^{6p}}\right)_{\mathrm{calc}}, \tag{8}$$

where the lower-case symbol denotes the hyperfine splitting constant for a single valence electron. For electronic states with $l > 0$, which are different in the principal quantum number n only, $b_2/b_0 = a_2/a_0$ [24] and Eq. (8) can be modified to

$$\left(\frac{B_2}{B_1}\right)_{\mathrm{calc}} = \left(\frac{B_0}{B_1}\right)_{\mathrm{ref}} \times \left(\frac{A_2}{A_1}\right)_{\mathrm{exp}} \times \left(\frac{A_1}{A_0}\right)_{\mathrm{ref}}. \tag{9}$$

Using the known reference values of A_0, B_0 ($^3P_2$) and A_1, B_1 ($^5S_2$) for ^{207}Po [23,25], the ratio $(B_2/B_1)_{\mathrm{calc}}$ was evaluated as 0.25(5).

C. Electromagnetic moments

The magnetic dipole μ and spectroscopic electric quadrupole Q_S moments were evaluated from the scaling relations

$$\mu = \frac{A}{A_{\mathrm{ref}}} \frac{I}{I_{\mathrm{ref}}} \mu_{\mathrm{ref}} \quad \text{and} \quad Q_S = \frac{B}{B_{\mathrm{ref}}} Q_{S,\mathrm{ref}}, \tag{10}$$

using the values of nuclear spin, hyperfine coupling constants, and electromagnetic moments for the reference isotope ^{207}Po:

$$I_{\mathrm{ref}} = 5/2, \quad A_{\mathrm{ref}} = 564(1)\,\mathrm{MHz},$$

$$B_{\mathrm{ref}} = 367(7)\,\mathrm{MHz}\ [23],$$

$$\mu_{\mathrm{ref}} = 0.793(55)\,\mu_N\ [26],$$

$$Q_{S,\mathrm{ref}} = 0.28(3)\,\mathrm{b}\ [25].$$

Expression (10) disregards any hyperfine anomaly. The uncertainty in $Q_{S,\mathrm{ref}}$ in Ref. [25] is not given directly, but according to the text should be at least 10%. The value of $Q_{S,\mathrm{ref}}$ should also be corrected for the Sternheimer effect [27]:

$$Q_S^{\mathrm{corr}} = \frac{Q_S^{nl}}{1 - R_{nl}}, \tag{11}$$

where Q_S^{nl} is the nuclear quadrupole moment deduced from the quadrupole splitting under the assumption that the electron core is spherical, R_{nl} is the quadrupole shielding factor. The shielding factor can be estimated as $R_{6p} = -0.20(5)$, based on the calculations for similar electronic configurations [28–30].

For an axially deformed nucleus the intrinsic quadrupole moment Q_0 can be evaluated from the spectroscopic quadrupole moment using the following expression:

$$Q_S = \frac{3\Omega^2 - I(I+1)}{(I+1)(2I+3)} Q_0, \tag{12}$$

where Ω is the projection of the nuclear spin on the symmetry axis of the nucleus. For well deformed nuclei in a strong-coupling assumption, $\Omega = I$.

The intrinsic quadrupole moment Q_0, induced by the nonspherical charge distribution of the protons, is then related to the nuclear static deformation β_2 by

$$Q_0 \approx \frac{3}{\sqrt{5\pi}} eZR_0^2 \left(\beta_2 + \frac{2}{7}\sqrt{\frac{5}{\pi}}\beta_2^2 + \cdots\right), \tag{13}$$

where the nuclear radius R_0 is usually calculated as $1.2\,A^{1/3}$ fm [31].

The deformation can also be estimated from the nuclear mean-square charge radii $\langle r^2\rangle_A$ using the expression

$$\langle r^2\rangle_A \approx \langle r^2\rangle_A^{\mathrm{sph}} \left(1 + \frac{5}{4\pi}\langle\beta_2^2\rangle_A\right), \tag{14}$$

where $\langle r^2\rangle_A^{\mathrm{sph}}$ is the mean-square radius of a spherical nucleus with the same volume [24]. For the evaluation of $\langle r^2\rangle_A^{\mathrm{sph}}$, the droplet model with a revised parametrization (second parameter set) [32] was used. The deformation deduced from the charge radii data with the aid of the droplet model will be denoted as DM deformation.

In contrast to the static deformation parameter β_2, the mean-square form $\langle\beta_2^2\rangle$ can be also related to the dynamic deformation (vibration) and diffuseness of the nucleus [33].

IV. RESULTS AND DISCUSSION

The hfs coupling constants obtained from the fits and the deduced nuclear moments are shown in Table I.

TABLE I. Measured values of the hyperfine splitting constants (A and B), deduced values of the the magnetic moment μ and spectroscopic electric quadrupole moment Q_S and the estimation of the quadrupole deformation parameter $\langle\beta_2^2\rangle^{1/2}$.

Isotope[a]	I^{π}[b]	A (GHz)	B (GHz)	μ[c] (μ_N)	μ_{lit}[cd] (μ_N)	Q_S[c] (b)	$\langle\beta_2^2\rangle^{1/2}$[e]
^{193ls}Po	$(3/2^-)$	−0.461(30)	−2.062(20)	−0.389(25){37}		−1.31(15){30}	0.21
^{193hs}Po	$(13/2^+)$	−0.203(10)	+1.71(40)	−0.742(40){65}		+1.08(30){50}	0.22
^{195ls}Po	$(3/2^-)$	−0.713(15)	−1.37(20)	−0.601(13){42}		−0.87(15){25}	0.18
^{195hs}Po	$(13/2^+)$	−0.255(10)	+2.02(40)	−0.932(40){65}		+1.30(30){45}	0.18
^{197}Po	$(3/2^-)$	−1.046(15)	−0.69(20)	−0.882(13){65}		−0.44(15){20}	0.13
^{197m}Po	$(13/2^+)$	−0.288(5)	+1.99(40)	−1.053(20){75}		+1.26(30){45}	0.13
^{199}Po	$(3/2^-)$	−1.081(10)	−0.43(15)	−0.912(10){65}		−0.27(12){15}	0.09
^{199m}Po	$(13/2^+)$	−0.275(10)	+2.20(25)	−1.005(40){70}	(−)0.987(30){73}	+1.40(20){35}	0.12
^{201}Po	$3/2^-$	−1.166(20)	+0.15(10)	−0.984(10){70}	(−)0.941(55){84}	+0.10(8){10}	0.10
^{201m}Po	$13/2^+$	−0.274(20)	+1.98(25)	−1.002(55){70}	(−)0.996(38){75}	+1.26(20){35}	0.12
^{203}Po	$5/2^-$	+0.527(10)	+0.27(10)	+0.741(15){52}	(+)0.739(25){56}	+0.17(8){10}	0.08
^{203m}Po	$13/2^+$	−0.264(10)	+1.92(10)	−0.965(40){67}		+1.22(10){20}	0.11
^{211}Po	$9/2^+$	−0.473(12)	−1.20(10)	−1.197(30){85}		−0.77(8){15}	0.12

[a] ^{209}Po is not shown in the Table because it was used only for calibration of the ratio of the magnetic coupling constants for ground and excited atomic states (see Sec. III B).
[b] Reference [34].
[c] The errors in parentheses reflect only the statistical experimental uncertainties; the total errors (including the systematic errors, which stem from the scaling uncertainties of the reference values of μ_{207} and $Q_{S,207}$) are given in the curly brackets.
[d] Reference [35].
[e] Estimation based on our data on the charge radii [11].

Figure 7 presents the magnetic moments obtained for the $3/2^-$ and $13/2^+$ states of $^{193-203}$Po in this work, along with the values for the heavier polonium isotopes. The magnetic moments for lead, mercury, and platinum isotopes are also shown for comparison. The magnetic moments of the $3/2^-$ and $13/2^+$ states of the polonium isotopes with $N \geqslant 113$ follow the trend observed in lead (and mercury for $13/2^+$ isomers) and are close to the calculated single-particle values for the almost spherical ^{207}Pb ($\mu_{sp}\{\nu i_{13/2}\} = -1.144\ \mu_N$, $\mu_{sp}\{\nu p_{3/2}\} = -1.227\ \mu_N$ [36]). For the magnetic moments of the light polonium isotopes with $N < 113$ (both low- and high-spin states) a deviation from the constant trend of the heavier isotopes is observed. Similar deviation can be seen in the behavior of the charge radii of polonium isotopes, which follow the spherical droplet-model predictions rather closely down to ^{199}Po ($N = 115$), but in the region $107 \leqslant N < 113$ a deviation from the linear trend for the heavier isotopes is also observed [10,11].

The trends of spectroscopic quadrupole moments for the $3/2^-$ and $13/2^+$ states of $^{193-203}$Po isotopes differ considerably, which is illustrated by Fig. 8. While the quadrupole moment of the $13/2^+$ isomers remains nearly constant for

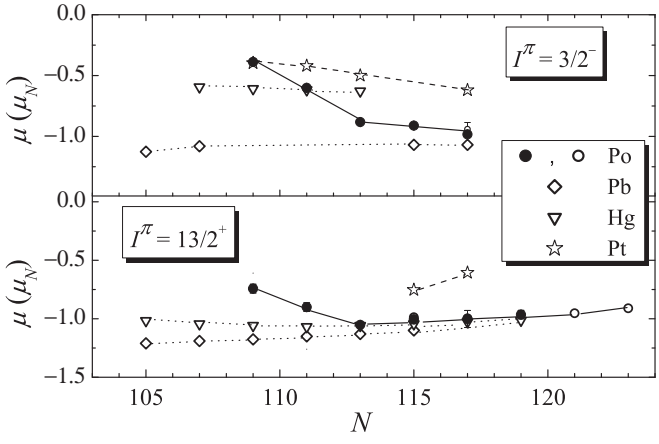

FIG. 7. Magnetic dipole moments for the neutron-deficient odd-A polonium, lead, platinum, and mercury isotopes. Data from this work are shown with filled circles, data from Refs. [35,37] with the open circles, and magnetic dipole moments for mercury, lead and platinum are taken from Refs. [6,8,38–45]. The lines connecting the data points are to guide the eye only.

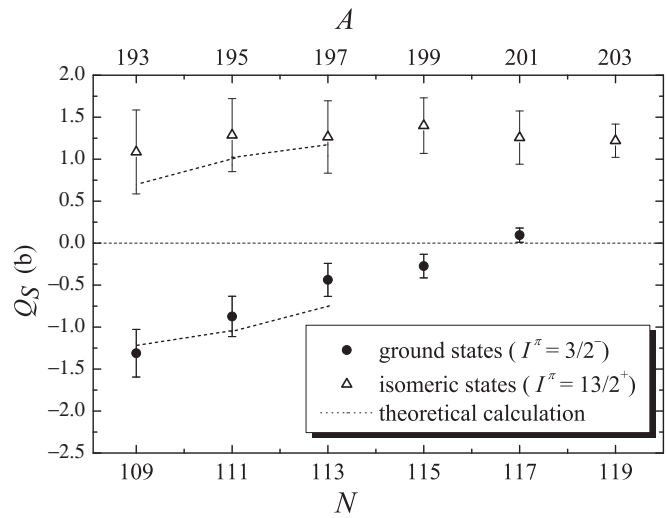

FIG. 8. Spectroscopic quadrupole moments for $^{193-203}$Po. The PPR-model predictions (see text) are shown with dotted lines.

$193 \leqslant A \leqslant 201$, a linear downward trend is found for the $3/2^-$ states.

A. Calculations of quadrupole moments with particle-plus-rotor model

The experimental values of the electromagnetic moments were compared with theoretical calculations. Calculations were made with the particle-plus-rotor (PPR) model [46] using an axially deformed Nilsson potential and the BCS approximation for pairing description [47]. The deformation was fixed to the DM-deformation values obtained in our previous work [11] (see Table I). The moment of inertia was calculated using the Grodzins-Raman formula [31] with the same deformation. The calculations were made for odd-A Po nuclei with $A < 198$ as this is the point where the marked deviation from sphericity occurs [10,11] and therefore the PPR model is applicable.

According to the calculations, the single particle structure of the moderately deformed odd-A polonium nuclei is characterized by strong mixing (by Coriolis interaction) of several Nilsson states with different spin projections on the symmetry axis Ω. The relation between spectroscopic and intrinsic quadrupole moment is described in this case by the following formula:

$$Q_S = \sum_i c_i^2(\Omega_i)\frac{3\Omega_i^2 - I(I+1)}{(I+1)(2I+3)}Q_0, \qquad \Omega_i = I, I-1, I-2, \ldots, \tag{15}$$

where c_i is the expansion coefficient of the wave function in the strong coupling basis, and Ω_i is the projection of the odd particle angular momentum of the given orbital on the symmetry axis.

For $13/2^+$ states in ^{193,195,197}Po Coriolis mixing is rather high and Q_S becomes positive although Q_0 (and associated deformation) is negative. For the relatively strongly deformed ^{193}Po and ^{195}Po the leading configuration is the 7/2[633] Nilsson state.

This simple model describes the quadrupole moments for these states fairly well (see Fig. 8, where the experimental and theoretical values of Q_S are presented). It is worth noting that for high-spin states $[I^\pi = (13/2^+)]$ in ^{193,195,197}Po the Q_S values can be calculated for the other possible spin assignments. The calculated values are not in an agreement with the experimental ones. For example, for ^{195}Po $Q_{S,\mathrm{theor}}^{11/2+} = +0.23$ b and $Q_{S,\mathrm{theor}}^{9/2+} = +0.19$ b, while the experimental values deduced with the same spin and parity assignment are +1.30(30) b and +1.21(30) b, respectively. This can be considered as additional evidence supporting the spin assignment $I^\pi = 13/2^+$ for the high-spin states in ^{193,195,197}Po.

The good description of quadrupole moments of the high-spin polonium isomers with $A = 193,195,197$ in the framework of the simple PPR-model with DM deformations confirms the conclusion of Ref. [48] in favor of the rotationally aligned scheme for an $i_{13/2}$ neutron hole and an oblate core.

For the $3/2^-$ states in ^{193,195,197}Po (for which Coriolis mixing is almost negligible) the values of the deformation parameters β_2 deduced from Q_S^{exp} in a strong-coupling assumption [see Eqs. (12) and (13)] are in good agreement with the values of $\langle\beta_2^2\rangle^{1/2}$ extracted from $\langle r^2\rangle$ and with the $\langle\beta_2^2\rangle^{1/2}$ extracted from $B(E2)$ values for adjacent even-A isotopes [49,50], as shown in Fig. 9. Theoretical values of Q_S are in agreement with the experimental values (see Fig. 8).

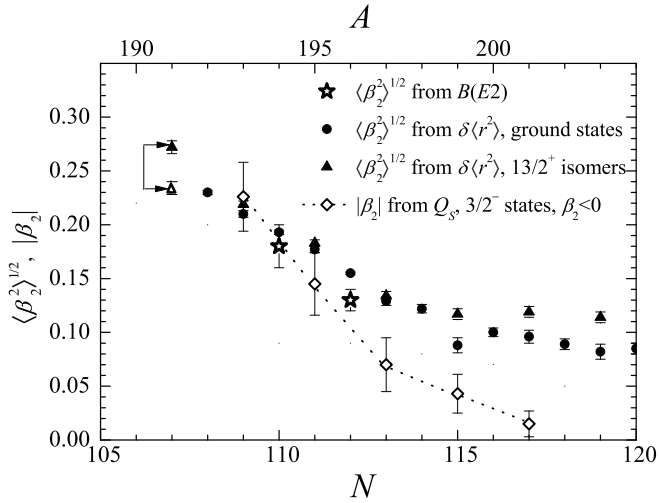

FIG. 9. Deformation parameters extracted from the charge radii, quadrupole moments, and $B(E2)$ values [49,50]. For ^{191}Po results of the fits with $B > 0$ and $B < 0$ are shown with the filled and unfilled triangles, respectively.

The quadrupole moments of neutron-deficient polonium isotopes ($A = 193,195,197$) are well described with the assumption of moderate permanent oblate deformation.

B. Deformation of neutron-deficient polonium isotopes in configuration-mixing method

The changes in the charge radii of adjacent even-A polonium isotopes are well reproduced (see Ref. [10]) in the framework of angular-momentum projected configuration-mixing method [51]. The close similarity of the level structure built on top of the isomeric $13/2^+$ state in the odd-A polonium nuclei and yrast levels of the corresponding even-A Po nuclei [48,52,53] indicates a coupling of the $i_{13/2}$ neutron to the states of the yrast band of the neighboring even-A core. Therefore the conclusions made on the base of the theoretical description of the even-A Po nuclei can be applied to their odd-A neighbors. In the configuration-mixing method the ground-state wave function is calculated by mixing mean-field states corresponding to different intrinsic axial quadrupole deformations. The result of these calculations is critically dependent on the choice of effective interaction. As in Refs. [50,54], at least for ^{194,196}Po (core nuclei for ^{195,197}Po) the ground-state wave function, calculated by this model (employing the Skyrme interaction SLy6 and a density-dependent pairing interaction), is nearly equally distributed around the spherical point at small prolate and oblate deformations, with a slight enhancement on the oblate side. The resulting ground-state mean deformation $\langle\beta_2\rangle < 0.05$ for ^{194,196}Po (see Fig. 5 in Ref. [50] and Fig. 9 in Ref. [54]) and does not explain the observed quadrupole moments in adjacent odd-A polonium nuclei. It should be noted

that at the same time the deduced mean-squared deformations for these ground-state wave function are sufficiently large $\langle\beta_2^2\rangle^{1/2} \approx 0.15$ to describe qualitatively the deviation from sphericity in charge radii of polonium isotopes with $A < 198$ [10,11]. It is shown in Ref. [54] that the configuration-mixing model with SLy6 interaction describes rather well the level structure of ^{194}Po and its transitional Q_t values apart from $Q_t(2^+)$. As pointed out in Ref. [54], the small value obtained for $Q_t(2^+)$ can be traced back to a deficiency in the description of the 0^+ ground state with the wave function, which has nearly equal oblate and prolate components.

In contrast to a nearly zero mean deformation in the ground state of ^{194,196}Po, predicted in Refs. [50,54], the dominance of an oblate deformation in the ground states of ^{192,194,196}Po was predicted in Ref. [55], where a configuration-mixing method similar to that of Ref. [48] with the Skyrme interaction SLy4, but without projection on angular momentum, was applied. The mean deformation of the ground state increases when going from ^{196}Po ($\beta_2 \approx -0.1$) to ^{192}Po ($\beta_2 \approx -0.2$) [55] which closely corresponds to the mean-squared deformations extracted from the charge radii [10] and explains the observed deviation from sphericity. The calculations in the framework of the same configuration-mixing method with the Skyrme interactions SLy4 and SLy4* and projection on angular momentum and particle number produce similar results [10].

From the measured quadrupole moments Q_S it can be concluded that the mean deformation of the lightest polonium isotopes ($A < 196$) increases, which appears consistent with calculations using the SLy4 interaction but not with results using the SLy6 interaction. It can be concluded that it is the increase of the mean deformation that governs both the deviation from sphericity in $\delta\langle r^2\rangle$ behavior of odd- and even-A polonium isotopes [10,11] and the observed trends in odd-A Po quadrupole moments. Although within the framework of configuration-mixing method, one cannot assign an intrinsic deformation to the wave functions, it is the well defined mean deformation that may "play the role" of intrinsic deformation, as shown by simple PPR calculations of quadrupole moments. The increasing mixing of oblate and nearly spherical configurations of the ground states of the light even-A polonium isotopes is confirmed by in-beam and α-decay data [56,57]. Similar to the even-A polonium nuclei, the decay pattern of the odd-mass isotopes ^{193m,g,195m,g}Po is also understood as a result of the mixing of the deformed (oblate) and the normal configurations in the parent polonium nuclei (see Refs. [9,48,52], and references therein).

C. Phenomenological estimation of configuration mixing and magnetic moments of neutron-deficient polonium isotopes

In a more phenomenological approach the mixing of the oblate and near-spherical configurations in even-A Po nuclei was estimated using different experimental observables (see Ref. [52], and references therein). According to Ref. [52] the mixing amplitude of the deformed state α^2 in the 0_1^+ ground state increases from 45% in ^{194}Po to 73% in ^{192}Po (calculated using a two-level mixing model). In Ref. [9] the following mixing amplitudes are proposed using the two-level mixing model: $\alpha^2(^{192}\text{Po}) = 0.58$, $\alpha^2(^{194}\text{Po}) = 0.29$, $\alpha^2(^{196}\text{Po}) = 0.11$. Estimations using an α-decay mixing model give $\alpha^2(^{192}\text{Po}) = 0.63$ [58]. Finally, in Ref. [59] both models were applied: $\alpha^2(^{192}\text{Po}) = 0.45$, $\alpha^2(^{194}\text{Po}) = 0.26$, $\alpha^2(^{196}\text{Po}) = 0.14$ (two-level mixing model) and $\alpha^2(^{192}\text{Po}) = 0.57$, $\alpha^2(^{194}\text{Po}) = 0.32$, $\alpha^2(^{196}\text{Po}) = 0.02$ (α-decay mixing model).

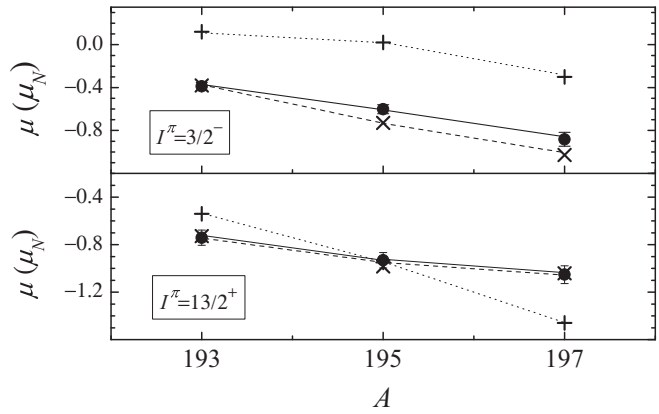

FIG. 10. Comparison of experimental and calculated magnetic moments for odd-A Po low- and high-spin states. Experimental data are shown with the filled circles, magnetic moments calculated in the PPR model with DM deformation are shown with the dotted line, and calculated magnetic moments that take into account mixture of near-spherical and deformed configurations [see Eq. (16)] are shown with the dashed line. The lines connecting the data points are to guide the eye only.

As shown in Fig. 10, the trends in the magnetic moments for low-spin and high-spin polonium isotopes are also well reproduced by the PPR calculations. However, there is a discrepancy between the theoretical predictions and the experimental values of magnetic moments for $I = 3/2$ isomers. The mixing of deformed and near-spherical configurations may be the reason for this discrepancy as the magnetic moments for near-spherical Pb and Po ($A > 199$) nuclei with $I = 3/2$ are significantly lower than those for the corresponding deformed Hg and Pt nuclei (see Fig. 7; compare also the single-particle value $\mu_{sp}\{\nu p_{3/2}\} = -1.227\ \mu_N$ calculated in Ref. [36]).

In a simple approximation magnetic moment of a mixed state can be estimated as

$$\mu = \alpha^2 \mu_{\text{def}} + (1 - \alpha^2)\mu_{\text{sph}}, \tag{16}$$

where μ_{def} is calculated within the PPR approach (see above) and μ_{sph} is the magnetic moment of the neighboring near-spherical odd-neutron nuclei with the same spin. Mixing amplitudes for ^{193,195,197}Po have been fixed in accordance with the mean values of mixing amplitudes for their even cores (taking into account all estimations of these coefficients cited above): $\alpha^2(^{193}\text{Po}) = 0.59$, $\alpha^2(^{195}\text{Po}) = 0.33$, $\alpha^2(^{197}\text{Po}) = 0.09$. For the estimation of μ_{sph}, magnetic moments of near-spherical Pb states with the same spins were used: $\mu_{\text{sph}}^{3/2-} = -1.1\ \mu_N$, $\mu_{\text{sph}}^{13/2+} = -1.0\ \mu_N$. The magnetic moments values calculated with these parameters, are shown in Fig. 10. It should be noted that the variation of the mixing amplitudes, obtained with the aid of different models and assumptions (see values

cited above) as well as the reasonable changes of $\mu_{\rm sph}$ ($-\{0.9-1.2\}\,\mu_N$) does not affect significantly the overall agreement of calculated and observed magnetic moments. This agreement (for both spins) supports the assumption of an increasing admixture of deformed configurations in the ground and long-lived isomeric states of polonium isotopes and preservation of the nonzero admixture of the near-spherical state when going from $N = 113$ to $N = 109$. This conclusion is consisted with the assumption of the increase in mean deformation in polonium nuclei with the decrease of N, made on the basis of the charge radii and quadrupole moments analysis.

It should be stressed that all conclusions made with the aid of this model-dependent approach are tentative. To obtain a consistent picture of the shape evolution in the light Po nuclei, all observables (Q, μ, $\delta\langle r^2\rangle$) should be treated in the framework of a single theoretical approach, covering both odd- and even-A nuclei.

V. SUMMARY

Hyperfine splitting parameters were measured for the neutron-deficient odd-A polonium isotopes $^{193-203}$Po^{g,m} and ^{209,211}Po. The electromagnetic moments μ and Q_S were deduced. For the most neutron-deficient nuclei ($A = 193,195,197$) the deviation of μ and Q_S from the nearly constant values for heavier polonium nuclei was observed. This deviation was explained by the mixing of deformed and near-spherical configurations starting from $A = 196,197$ and the strong Coriolis mixing at moderate deformation for the high-spin odd Po isomers.

The assumption of gradual increase in a mean deformation of the mixed states (with decreasing of N from 113 to 109) seems to be necessary to explain the $\delta\langle r^2\rangle$ values [10,11] as well as behavior of the electromagnetic moments Q_S and μ. These conclusions are in good agreement with the picture of the shape evolution in the light polonium isotopes presented in Ref. [48].

ACKNOWLEDGMENTS

We would like to thank the ISOLDE Collaboration for providing excellent beams and the GSI Target Group for manufacturing the carbon foils. This work was supported by FWO-Vlaanderen (Belgium), by GOA/2004/03 (BOF–K.U. Leuven), by the IUAP–Belgian State Belgian Science Policy (BriX network P7/12), by the European Commission within the Sixth Framework Programme through I3-EURONS (Contract No. RII3-CT-2004-506065), by the U.K. Science and Technology Facilities Council, and by the Slovak Research and Development Agency (Contract No. APVV-0105-10).

[1] K. Heyde, P. Van Isacker, M. Waroquier, J. L. Wood, and R. A. Meyer, Phys. Rep. **102**, 291 (1983).
[2] J. L. Wood, K. Heyde, W. Nazarewicz, M. Huyse, and P. Van Duppen, Phys. Rep. **215**, 101 (1992).
[3] A. N. Andreyev *et al.*, Nature (London) **405**, 430 (2000).
[4] R. Julin, K. Helariutta, and M. Muikku, J. Phys. G **27**, R109 (2001).
[5] K. Heyde and J. L. Wood, Rev. Mod. Phys. **83**, 1467 (2011).
[6] G. Ulm *et al.*, Z. Phys. A **325**, 247 (1986).
[7] H. De Witte *et al.*, Phys. Rev. Lett. **98**, 112502 (2007).
[8] M. D. Seliverstov *et al.*, Eur. Phys. J. A **41**, 315 (2009).
[9] N. Bijnens *et al.*, Phys. Rev. Lett. **75**, 4571 (1995).
[10] T. E. Cocolios *et al.*, Phys. Rev. Lett. **106**, 052503 (2011).
[11] M. D. Seliverstov *et al.*, Phys. Lett. B **719**, 362 (2013).
[12] E. Kugler, Hyperfine Interact. **129**, 23 (2000).
[13] V. N. Fedosseev *et al.*, Nucl. Instrum. Methods B **266**, 4378 (2008).
[14] V. N. Fedosseev *et al.*, Rev. Sci. Instrum. **83**, 02A903 (2012).
[15] B. A. Marsh *et al.*, Hyperfine Interact. **196**, 129 (2010).
[16] T. E. Cocolios *et al.*, Nucl. Instrum. Methods B **266**, 4403 (2008).
[17] B. A. Marsh *et al.*, Nucl. Instrum. Methods B **317**, 550 (2013).
[18] B. Lommel, W. Hartmann, B. Kindler, J. Klemm, and J. Steiner, Nucl. Instrum. Methods A **480**, 199 (2002).
[19] T. E. Cocolios *et al.*, J. Phys. G **37**, 125103 (2010).
[20] J. Lettry, R. Catherall, P. Drumm, P. Van Duppen, A. H. M. Evensen, G. J. Focker, A. Jokinen, O. C. Jonsson, E. Kugler, H. Ravn, and the ISOLDE Collaboration, Nucl. Instrum. Methods B **126**, 130 (1997).
[21] T. E. Cocolios *et al.*, J. Phys. Conf. Ser. **381**, 012072 (2012).
[22] K. Hanke, Int. J. Mod. Phys. A **28**, 1330019 (2013).
[23] D. Kowalewska, K. Bekk, S. Göring, A. Hanser, W. Kälber, G. Meisel, and H. Rebel, Phys. Rev. A **44**, R1442(R) (1991).
[24] E. W. Otten, In *Treatise on Heavy-Ion Science*, edited by D. A. Bromley, Vol. 8 (Plenum, New York, 1989), p. 517.
[25] C. M. Olsmats, S. Axensten, and G. Liljegren, Ark. Fys. **19**, 469 (1961).
[26] P. Herzog, H. Walitzki, K. Freitag, H. Hildebrand, and K. Schlösser, Z. Phys. A **311**, 351 (1983).
[27] R. M. Sternheimer, Phys. Rev. **80**, 102 (1950).
[28] R. M. Sternheimer (private communication), as discussed in H.-P. Clieves *et al.*, Z. Phys. A **289**, 361 (1979).
[29] R. M. Sternheimer and R. F. Peierls, Phys. Rev. A **3**, 837 (1971).
[30] Y. Tanaka, R. M. Steffen, E. B. Shera, W. Reuter, M. V. Hoehn, and J. D. Zumbro, Phys. Rev. Lett. **51**, 1633 (1983).
[31] S. Raman, C. W. Nestor Jr., and P. Tikkanen, At. Data Nucl. Data Tables **78**, 1 (2001).
[32] D. Berdichevsky and F. Tondeur, Z. Phys. A **322**, 141 (1985).
[33] W. D. Myers and K. H. Schmidt, Nucl. Phys. A **410**, 61 (1983).
[34] Evaluated Nuclear Structure Data File (ENSDF), www.nndc.bnl.gov/ensdf/
[35] J. Wouters, N. Severijns, J. Vanhaverbeke, and L. Vanneste, J. Phys. G **17**, 1673 (1991).
[36] R. Bauer, J. Speth, V. Klemt, P. Ring, E. Werner, and T. Yamazaki, Nucl. Phys. A **209**, 535 (1973).
[37] P. Raghavan, At. Data Nucl. Data Tables **42**, 189 (1989).
[38] H. T. Duong *et al.*, Phys. Lett. B **217**, 401 (1989).
[39] Th. Hilberath, St. Becker, G. Bollen, H.-J. Klüge, U. Krönert, G. Passler, J. Rikovska, R. Wyss, and the ISOLDE Collaboration, Z. Phys. A **342**, 1 (1992).

[40] S. B. Dutta, R. Kirchner, O. Klepper, T. U. Kühl, D. Marx, G. D. Sprouse, R. Menges, U. Dinger, G. Huber, and S. Schröder, Z. Phys. A **341**, 39 (1991).
[41] P. Dabkiewicz, F. Buchinger, H. Fischer, H.-J. Kluge, H. Kremmling, T. Kühl, A. C. Müller, and H. A. Schuessler, Phys. Lett. B **82**, 199 (1979).
[42] R. J. Reimann and M. N. McDermott, Phys. Rev. C **7**, 2065 (1973).
[43] F. Bacon, G. Kaindl, H.-E. Mahnke, and D. A. Shirley, Phys. Rev. Lett. **28**, 720 (1972).
[44] G. Schütz, E. Hagn, P. Kienle, and E. Zech, Phys. Rev. Lett. **56**, 1051 (1986).
[45] D. Agresti, E. Kankeleit, and B. Persson, Phys. Rev. **155**, 1339 (1967).
[46] E. Osnes, J. Rekstad, and O. K. Gjøtterud, Nucl. Phys. A **253**, 45 (1975).
[47] I. Ragnarsson and R. K. Sheline, Phys. Scr. **29**, 385 (1984).
[48] A. N. Andreyev *et al*., Phys. Rev. C **66**, 014313 (2002).
[49] T. Grahn *et al*., Phys. Rev. Lett. **97**, 062501 (2006).
[50] T. Grahn *et al*., Phys. Rev. C **80**, 014323 (2009).
[51] M. Bender, P. Bonche, T. Duguet, and P.-H. Heenen, Phys. Rev. C **69**, 064303 (2004).
[52] K. Helariutta *et al*., Eur. Phys. J. A **6**, 289 (1999).
[53] D. R. Wiseman *et al*., Eur. Phys. J. A **34**, 275 (2007).
[54] T. Grahn *et al*., Nucl. Phys. A **801**, 83 (2008).
[55] N. A. Smirnova, P.-H. Heenen, and G. Neyens, Phys. Lett. B **569**, 151 (2003).
[56] K. Helariutta *et al*., Phys. Rev. C **54**, R2799 (1996).
[57] K. Van de Vel *et al*., Phys. Rev. C **68**, 054311 (2003).
[58] R. Allatt *et al*., Phys. Lett. B **437**, 29 (1998).
[59] K. Van de Vel, Ph.D. thesis, KU Leuven, 2003.